Self-Supported Cobalt Phosphide Mesoporous Nanorod Arrays: A Flexible and Bifunctional Electrode for Highly Active Electrocatalytic Water Reduction and Oxidation

*Yun-Pei Zhu, Yu-Ping Liu, Tie-Zhen Ren, and Zhong-Yong Yuan**

Water splitting for the production of hydrogen and oxygen is an appealing solution to advance many sustainable and renewable energy conversion and storage systems, while the key fact depends on the innovative exploration regarding the design of efficient electrocatalysts. Reported herein is the growth of CoP mesoporous nanorod arrays on conductive Ni foam through an electrodeposition strategy. The resulting material of well-defined mesoporosity and a high specific surface area (148 $m^2 g^{-1}$) can be directly employed as a bifunctional and flexible working electrode for both hydrogen and oxygen evolution reactions, showing superior activities as compared with noble metal benchmarks and state-of-the-art transition-metal-based catalysts. This is intimately related to the unique nanorod array electrode configuration, leading to excellent electric interconnection and improved mass transport. A further step is taken toward an alkaline electrolyzer that can achieve a current density of 10 mA cm^{-2} at a voltage around 1.62 V over a long-term operation, better than the combination of Pt and IrO_2. This development is suggested to be readily extended to obtain other electrocatalysis systems for scale-up water-splitting technology.

1. Introduction

Currently, water splitting through electrolysis and photoelectrochemistry involving cathodic hydrogen evolution reaction (HER) and anodic oxygen evolution reaction (OER) is of particular significance for the production of renewable hydrogen energy and the development of regenerative fuel cells and rechargeable metal-air batteries.[1–4] Note that overpotentials originating from the polarization phenomenon occurring at the electrodes induce a larger voltage window than the theoretical minimum one (1.23 V) to afford thermodynamic driving force.[5,6] As such, the sluggish apparent reaction kinetics necessitates the utilization of noble-metal-based electrocatalysts to achieve respectable performance, i.e., Pt for HER and IrO_2/RuO_2 for OER,[7,8] though the scarcity and the consequent unfavorable cost prohibit the scale-up deployment in energy devices. Accordingly, great efforts have been made toward efficient earth-enriched materials, such as OER catalysts working under strongly alkaline conditions and HER catalysts operating in strongly acidic mediums, due to the thermodynamic convenience and application prospect in alkaline electrolyzers or proton-exchange membrane.[9–15] On the one hand, pairing the OER and HER catalysts together in the same electrolyte is of practical values to accomplish overall water splitting, which remains difficult to achieve owing to the incompatibility of the stability and activity for the same catalyst systems in the operating pH regions, thereby leading to inferior efficiency; on the other hand, the different catalysts intended to separate HER and OER may need distinct synthetic strategies and instruments with low-throughput preparation processes.[16–20] Therefore, it is still a grand challenge to exploit bifunctional electrocatalysts in terms of not only featuring high efficiency toward both hydrogen and oxygen evolution reactions, but also simplifying the system and reducing the costs.

Transition Co-based catalysts have been regarded as promising alternatives to noble metals to drive the half reactions, for instance, metal Co,[21] CoS,[22] and CoSe,[23] for HER and Co oxides/(oxy)hydroxides designed for OER.[24,25] Indeed, CoO_x-carbon composites have been implemented to be bifunctional and effective electrocatalysts for overall water splitting in base, wherein the involvement of conductive carbonaceous hosts is to overcome the disadvantages of self-accumulation and insufficient electric conductivity as to oxides.[26,27] Nonetheless, the sophisticated preparation and instability of active phases in acid propose an obstacle to further optimize the technology and find

Y.-P. Zhu, Dr. Y.-P. Liu, Prof. Z.-Y. Yuan
Key Laboratory of Advanced Energy Materials Chemistry (Ministry of Education)
Collaborative Innovation Center of Chemical Science and Engineering (Tianjin)
College of Chemistry
Nankai University
Tianjin 300071, P. R. China
E-mail: zyyuan@nankai.edu.cn
Prof. T.-Z. Ren
School of Chemical Engineering and Technology
Hebei University of Technology
Tianjin 300130, P. R. China
Prof. Z.-Y. Yuan
National Institute for Advanced Materials
School of Materials Science and Engineering
Nankai University
Tianjin 300353, P. R. China

DOI: 10.1002/adfm.201503666

new bifunctional catalysts. Also, when prepared as thin films on glassy carbons or other types of substrates through time-consuming casting or coating procedures with the assistance of polymeric binders, the catalyst powders exhibit deteriorative performances due to circumvent bubble-releasing problems introduced by the hydrophobicity of carbon supports and weak adhesion and thus the easy peeling of the coated catalysts. Searching for an advanced electrode configuration with mechanical peculiarities represents an intriguing approach.

An optimal electrode structure accompanied with high-performance catalyst is prerequisite to reduce the evolution overpotentials and promote the reaction kinetics, thereby enhancing the energy efficiency. Self-supported electrocatalysts can be directly employed as electrodes associated with evaluated structural and electrical connection between the catalysts and electrode matrixes and the resulting high stability, providing new opportunities for improving the architectural properties for facile charge carrier transfer and gas transport.[10,28–35] Different current collectors endow the final electrodes with diverse peculiarities and uses, for example, transparent conductive glasses for photoelectrochemistry and bendable carbon-fiber papers for flexible devices,[36,37] meaning that judicious selection of the right substrate can contribute to an enhanced and synergistic performance, thus relaxing the stringent demands of intrinsic catalytic capability needed to realize a specific level of activity. Under this context, flexible electrode configurations featuring mechanical stability and complex nanostructures show robust durability for long-term utilization and enlarged catalytically active surface areas to present enhanced electrochemical activity in the real water splitting process. Noticeably, Co-phosphors species have recently been investigated as efficient electrocatalysts for water electrolysis, i.e., Co phosphides and phosphates for hydrogen and oxygen evolution,[38–42] respectively, with considerable activity and durability in a broad pH range. In spite of these crucial advances, the rational construction and design of flexible Co-phosphors-based self-supported electrodes with specified activity and mechanical properties, to the best of our knowledge, have been rarely reported.

Herein, we present an integrated electrode consisted of Co phosphide mesoporous nanorod arrays (CoP-MNA) through an electrodeposition methodology, avoiding the conventional phosphization treatment and alleviating the energy and environmental concerns. Because of the remarkable structural characteristics, the electrode not only can catalyze hydrogen evolution outperforming the state-of-the-art noble Pt benchmark with favorable kinetics, but also demonstrates competitive activity toward anodic oxygen production in comparison with the IrO_2 counterpart but with more robust durability. Additionally, this electrode with dual functionality enables a highly active alkaline full water electrolyzer without obvious degradation after a long-term operation, better than the coupled system of Pt and IrO_2.

2. Results and Discussion

2.1. Material Synthesis and Characterization

The CoP mesoporous nanorod arrays are fabricated via a potentiostat electrodeposition way in a three-electrode mode, in which Ni foam performs as the working electrode (see synthesis details in the Supporting Information). The highly conductive Ni foam permits the electron to continuously transfer through the whole framework, initializing the effective reduction of Co^{2+} and $H_2PO_2^-$ to give a net reaction to yield CoP.[43] The preliminarily formed CoP with good conductivity can facilitate the further nucleation,[44,45] causing the generation of CoP nanorods with synchronously emerged mesopores inside (**Scheme 1**).

Following the electrodeposition, the sliver-gray pristine Ni foam substrate turns to black (Figure S1, Supporting

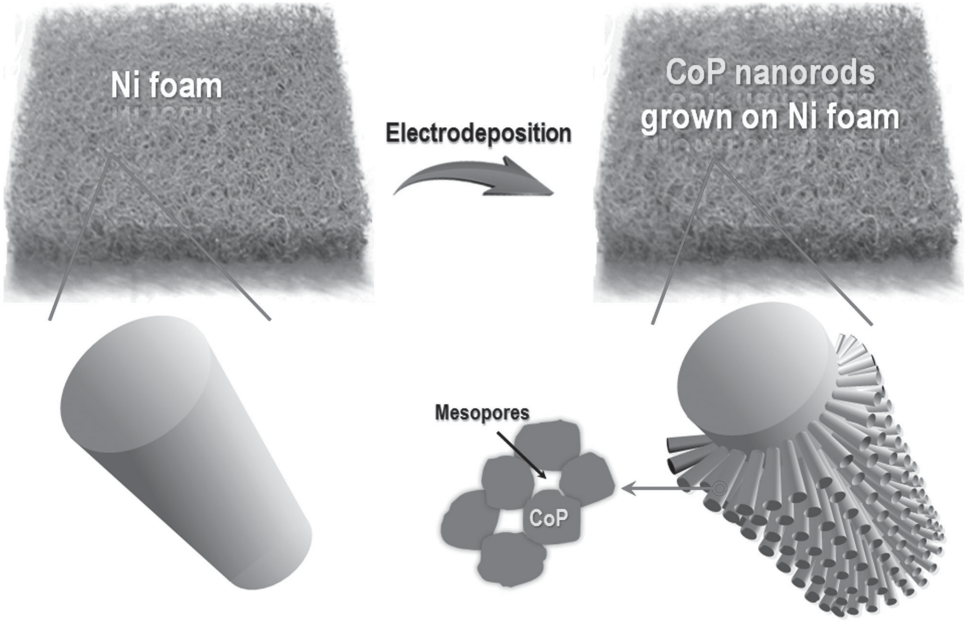

Scheme 1. Schematic illustration of the fabrication of CoP mesoporous nanorods arrays.

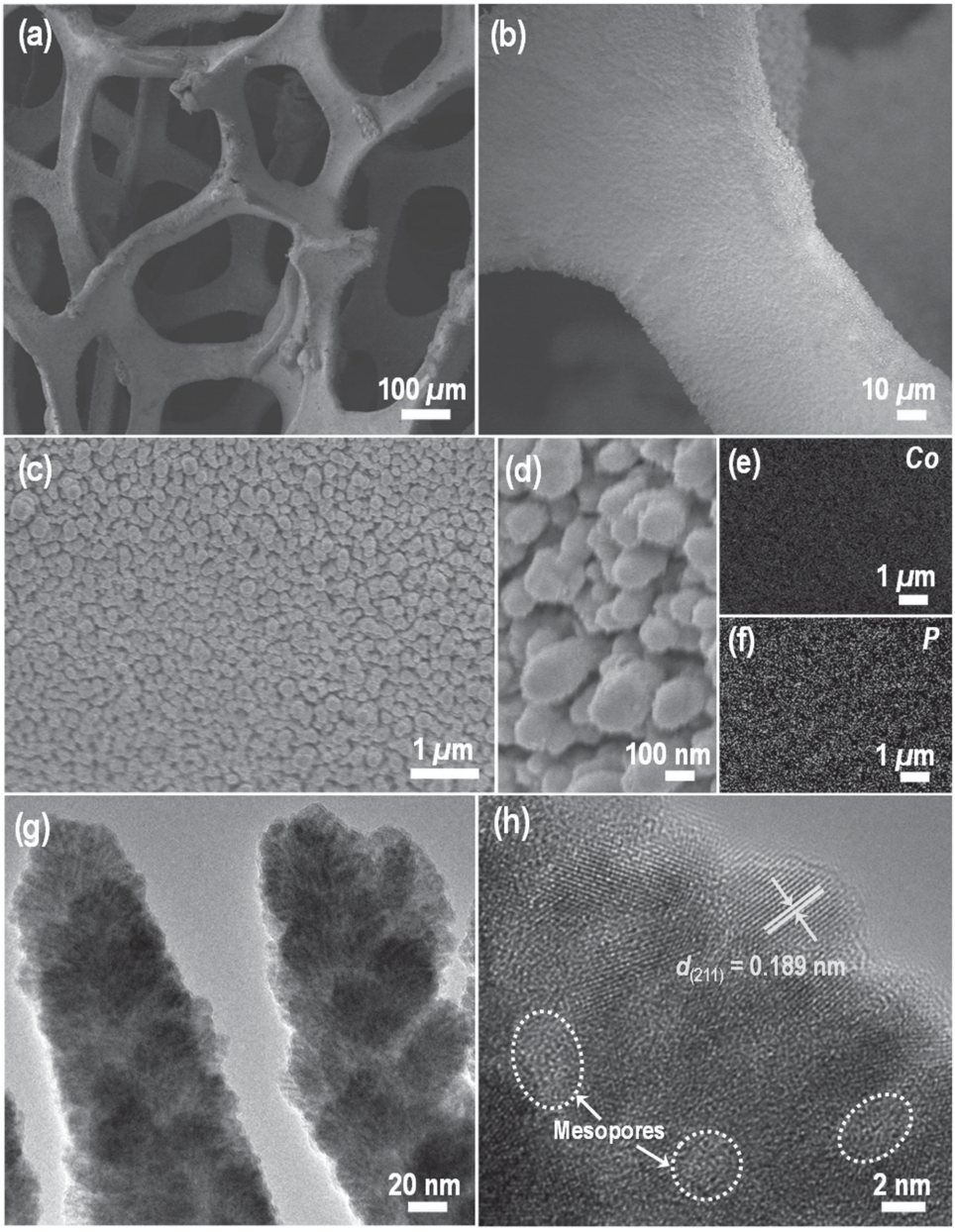

Figure 1. a–d) SEM, e,f) EDS elemental mapping, and g,h) TEM images of CoP-MNA.

Information). Upon inspection of the foam surface employing scanning electron microscopy (SEM), it can be observed that the macroporous morphology can be well retained (**Figure 1**a), while the surface become rougher as compared with the original one (Figure 1b and Figure S2, Supporting Information). Deeper magnification reveals that the rough surface is uniformly covered with a high-density array of vertically aligned nanorods with the diameter of 50–120 nm (Figure 1c,d). The energy dispersive X-ray spectroscopy (EDS) elemental mapping images in Figure 1e,f for CoP-MNA verify the homogeneous distribution of Co and P, confirming the uniform growth of CoP nanorods. The transition electron microscopy (TEM) image shows the uneven surface for the CoP nanorods (Figure 1g), and a closer look by high-resolution TEM (HR-TEM) (Figure 1h) presents different domains resulted from the tight aggregation of nanopartiles with a well-resolved lattice fringe space of 0.189 nm assigned to the (211) plane of CoP, leaving interpartical mesopores of several nanometers.

A series of diffraction peaks on the X-ray diffraction (XRD) pattern of CoP-MNA match well with orthorhombic CoP phase structure (JCPDS No. 29-0497) (**Figure 2**a). The weak diffraction intensity reveals the small size of CoP, well consistent with the TEM observation. The textual properties are assessed by N_2 adsorption–desorption analysis (Figure 2b). The N_2 sorption isotherm recorded on CoP-MNA is of typical type IV with a hysteresis loop of type H2, indicative of the existence of ink-bottle-like mesopores.[46] Correspondingly, the pore size distribution curve, calculated by the Barrett–Joyner–Halenda

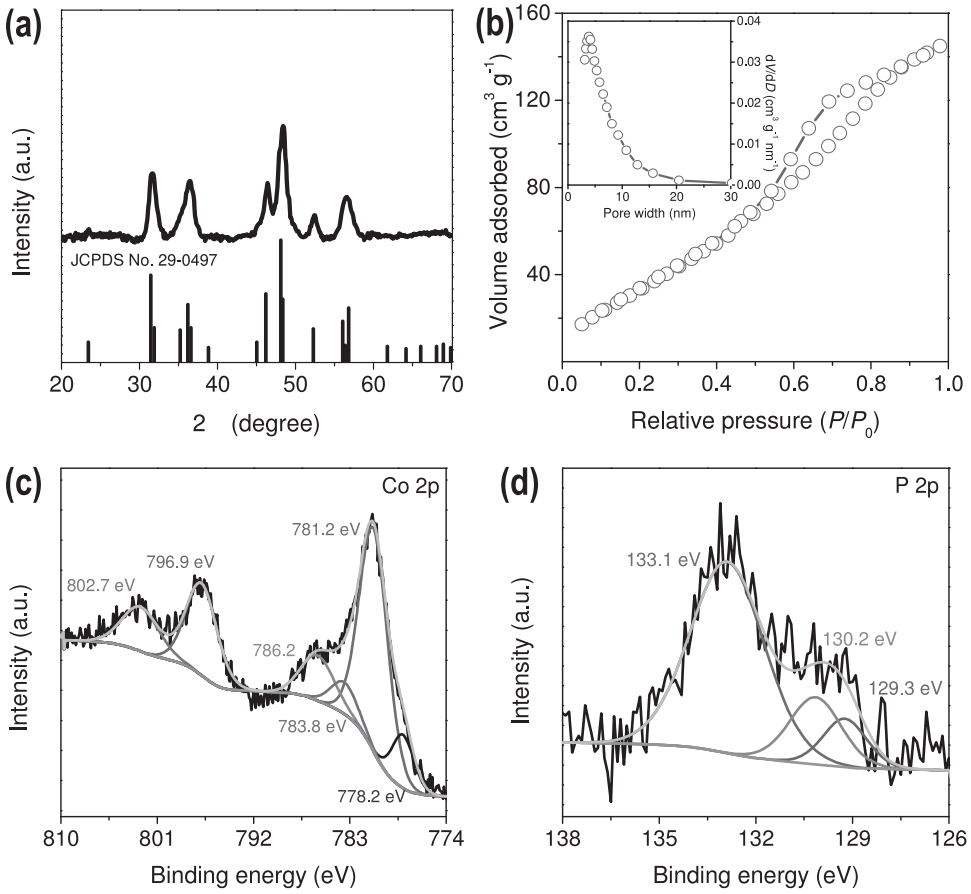

Figure 2. a) Wide-angle XRD pattern, b) N_2 sorption isotherm. Inset: the corresponding pore size distribution curve. c,d) High-resolution XPS spectra of the Co 2p and P 2p core levels for CoP-MNA.

(BJH) model, shows a maximum centered around 4 nm. The Brunauer–Emmett–Teller (BET) specific surface area is determined to be 148 m^2 g^{-1}, along with a total pore volume of 0.224 cm^3 g^{-1}, higher than that of other reported nanoarrays prepared through the conventional nucleation and thermal treatment (up to 100 m^2 g^{-1}),[47–49] suggesting the superiority of present mild and convenient methodology for creating nanoporous nanoarrays.

X-ray photoelectron spectroscopy (XPS) depth profile analysis is then utilized to analyze the surface chemistry of the CoP-MNA electrode. Peak deconvolution of the Co $2p_{3/2}$ core level region shows two main peaks at 778.2 and 781.2 eV and two satellites at 783.8 and 785.6 eV, respectively, while the Co $2p_{1/2}$ region shows one main peak at 796.9 eV accompanied with one satellite peak at 802.7 eV (Figure 2c). The intense satellite peaks in Co 2p spectra observed located at 785.6 and 802.7 eV can be ascribed to the shakeup excitation of the high-spin Co^{2+} ions.[50] For the high-resolution P 2p spectrum (Figure 2d), a weak doublet situated at 129.3 and 130.2 eV correspond to P $2p_{3/2}$ and P $2p_{1/2}$ lines, respectively, and another contribution at 133.6 eV can be assigned to oxidized phosphate species.[51] The peaks at 778.2 eV for Co $2p_{3/2}$ and 129.3 eV for P $2p_{3/2}$ are associated with the typical binding energies for Co 2p and P 2p contributions in CoP, respectively. All of these characterizations and analysis confirm the homogeneously allocated mesoporous CoP nanorods on conductive nickel matrix, which is designed for efficient electrocatalysts.

2.2. Hydrogen Evolution Activity

The electrodes with controllable size and shapes can be gained by simply tailoring the Ni foam, and the direct preparation of the CoP deposited on Ni foam allows for convenient investigation of the electrocatalytic activity for water splitting without additional binders and extra substrates (Figure S3, Supporting Information). The water electrolysis activity of the CoP-MNA is firstly evaluated by electrocatalytic hydrogen evolution using a classical three-electrode apparatus in strongly alkaline media (1 M KOH) that is continuously purged with H_2. Polarization curves from linear sweep voltammetry (LSV) tests display the geometric current density (J) plotted against the potential with respect to reversible hydrogen electrode (RHE) for the CoP-MNA bulk electrode (**Figure 3**a), as well as that of commercially available Pt foil standard and pristine Ni foam for the purpose of comparison. Pt foil exhibits outstanding activity toward HER, while bare Ni foam possesses quite weak catalytic activity before –0.3 V. In sharp contrast, the current recorded on CoP-MNA presents a small onset potential of nearly zero with tremendously enhanced cathodic current after further sweeping

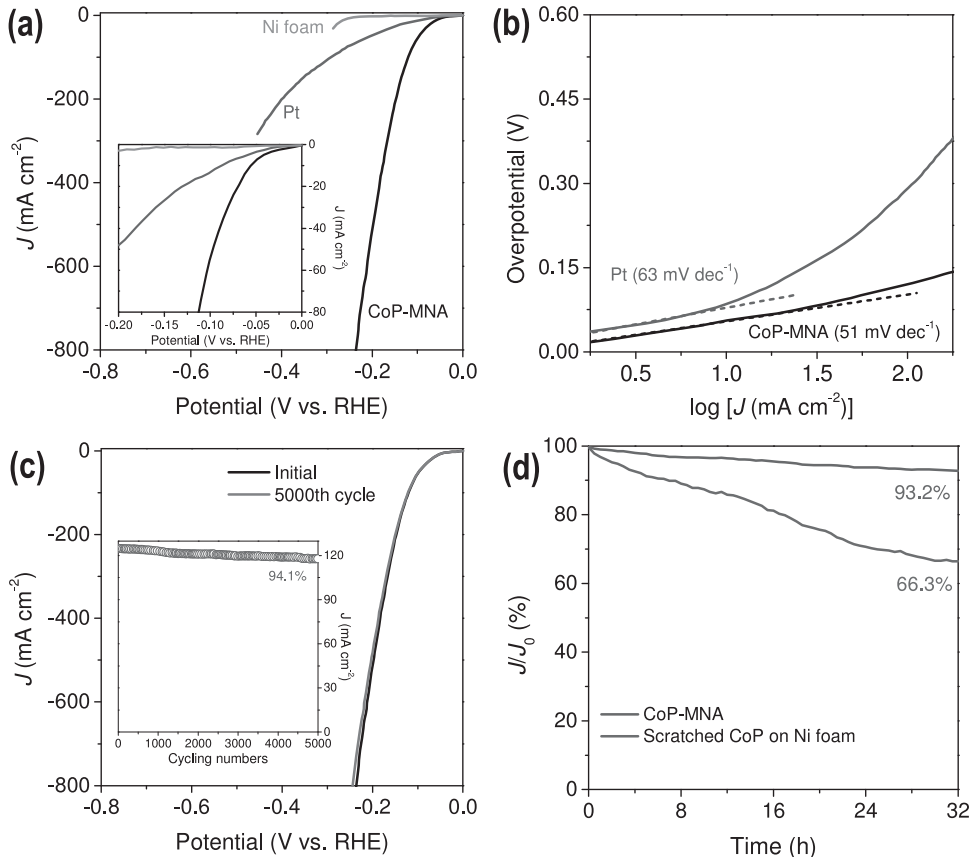

Figure 3. Electrochemical tests of CoP-MNA, Pt, pristine Ni foam, and scratched CoP postcoated on Ni foam electrodes for hydrogen evolution electrocatalysis. a) Polarization curves and b) Tafel plots of CoP-MNA, Pt, and pristine Ni foam in H_2-saturated 1 M KOH aqueous solution at a scan rate of 2 mV s^{-1}. c) Polarization curves of CoP-MNA initially and after 5000 CV scans (scan rate: 100 mV s^{-1}). Inset in (c): plot of current density recorded at –0.125 V versus cycle number. d) Chronoamperometric response curves of CoP-MNA and the counterpart of scratched CoP coated on Ni foam at a constant current of –0.1 V.

to negative applied potential, along with severe release of H_2 gas bubbles from the electrode surface (Video S1, Supporting Information), implying that the electrochemical deposition of CoP components can significantly improve the catalytic activity. It is notwithstanding that the HER performance for CoP-MNA largely exceeds that of noble Pt reference in the aspects of both onset potential and current behavior. Remarkably, CoP-MNA is able to render current densities of 10, 100, and 800 mA cm^{-2} at overpotentials (η) of 54, 121, and 235 mV, respectively, the excellent performance of which makes it obviously superior over all the reported Co-phosphors and various recently developed non-noble catalysts. A detailed comparison of HER performance for CoP-MNA with other highly active electrocatalyts with different electrode configurations is elaborated in Table S1 of the Supporting Information.

In addition, the reaction kinetics for hydrogen production can be revealed by the Tafel plots. The linear fitting of the Tafel curves renders a Tafel slope of 51 mV dec^{-1} for CoP-MNA, lower than that of Pt benchmark (63 mV dec^{-1}), indicating a more rapid reaction kinetics on CoP-MNA. The exchange current density for CoP-MNA, determined by extrapolation method on the basis of Tafel plot (Figure S4, Supporting Information), is calculated to be 0.857 mA cm^{-2}, which is largest among non-Pt-based HER electrocatalysts (Table S1, Supporting Information). Furthermore, it is of extraordinary importance to develop electrocatalyst that fulfill the qualifications of high performance in a broad pH range of aqueous electrolytes. In 0.5 M H_2SO_4, the CoP-MNA composite electrode shows inferior activity than the Pt foil before –0.17 V associated with a Tafel slope of 65 mV dec^{-1}, beyond which point CoP-MNA features a much better performance (Figure S5, Supporting Information). Owing to the relatively sluggish hydrogen evolution kinetics in neutral media (0.5 M PBS),[21,52] CoP-NP performs as less active catalysts as compared with that in strongly acidic or base solutions, but still excels noble platinum (Figure S6, Supporting Information).

The HER pathway in alkaline electrolyte generally follows the Volmer–Tafel or Volmer–Heyrovsky mechanisms[53,54]

$$\begin{aligned} &H_2O + e^- \rightarrow H_{ads} + OH^- \text{(Volmer) and} \\ &H_2O + H_{ads} + e^- \rightarrow H_2\uparrow + OH^- \text{(Heyrovsky)} \end{aligned} \quad (1)$$

$$\begin{aligned} &H_2O + e^- \rightarrow H_{ads} + OH^- \text{(Volmer) and} \\ &H_{ads} + H_{ads} \rightarrow H_2\uparrow \text{(Tafel)} \end{aligned} \quad (2)$$

wherein both pathways involve the adsorption of H_2O molecules and the corresponding electrochemical dissociation of

captured H_2O into adsorbed H atoms (H_{ads}) and OH^- species, followed by the detachment of OH^- to refresh the surface and formation of adsorbed H intermediates to yield H_2. The charge unbalance of Co and P, due to the transfer of electron density from Co to P,[51,55] can facilitate the adsorption of OH^- from H_2O decomposition on locally positively charged Co centers as the strong electrostatic affinity, while the nearby P sites prefer H adsorption, both of which the impart enhanced HER catalytic activity. The evidently worse activity in acid than that in base for CoP-MNA tentatively suggests that the generation and desorption of OH^- may be a vital step for hydrogen evolution in alkaline condition.[19]

Electrochemical impedance spectrum (EIS) analysis under operating conditions is conducted to probe the HER kinetics occurring at the electrode/electrolyte interface. The charge transfer resistance (R_{CT}) related to the electrocatalytic kinetics can be determined from the diameter of the semicircles in the low frequency zone. The larger the overpotential is, the smaller R_{CT} is (Figure S5, Supporting Information), due to accelerated electron transfer capability under increasing cathodic bias. The Tafel slope, derived from the plot of log (R_{CT}^{-1}) versus η, is 58 mV dec^{-1}, slightly lower than that extracted from the LSV polarization curve (65 mV dec^{-1}) on account of exclusion the contributions from the catalyst resistance, signifying a considerably small electron transport resistance in the composite electrode.[56] It should be noted that the direct deposition of active components on highly conductive 3D Ni foam can effectually improve electron transfer from the host substrate to CoP due to the intimate mechanical adhesion. This is further confirmed by a control electrode that is prepared by scratching down CoP and then reloading it onto Ni foam with the use of Nafion binder, which manifests poorer HER activity needing an overpotential of 252 mV to attain 100 mA cm^{-2} (Figure S7, Supporting Information).

Another critical criterion to evaluate the electrocatalysts is the long-term stability. Accelerated degradation studies after continuous cyclic voltammogram (CV) scanning for 5000 cycles in 1 M KOH at a scan rate 100 mV s^{-1} illustrates only 6.8% cathodic current loss (Figure 3d), suggesting the prominent ability of CoP-MNA to withstand accelerated electrochemical process. Further, the chronoamperometric response displays the high durability of the CoP-MNA electrode, which maintains considerable activity with a slight cathodic current attenuation of 6.5% within 32 h, whereas the sample prepared by post-coating of scratched CoP on Ni foam exhibits a disadvantaged current decay over a long period of test, attributable to the superiority of active materials directly grown on current collectors over the post-coated electrocatalysts on the electrode substrate (Figure S7, Supporting Information),[4,10,57] wherein the latter suffer from the abscission of catalysts resulted from the evolution of large amounts of hydrogen.

The nature of conductive matrixes enables the feasible design of smart devices because of the structural and mechanical features. For instance, the current density in the hydrogen evolution region for CoP-MNA is not susceptible to the scan rate (**Figure 4**a), demonstrating a little variation of 5.5% with the increase of scan rate from 2 to 100 mV s^{-1}, mainly benefiting from that the macroporous framework of Ni foam and mesopores in the nanorods can guarantee fast mass transport. Moreover, the three-dimensional architecture of CoP-MNA and the microstructure of regular CoP mesoporous nanorods are believed to provide loose textures and open spaces that are of positive influence to boost the release of evolved gas bubbles and the instant diffusion of electrolyte to take full advantage of active sites in CoP. On the other side, CoP-MNA preserves the interconnected networks of the original Ni foam and thus the good flexibility (Figure 4b). In order to investigate the potentiality for flexible energy conversion systems, the CoP-MNA undergoes various deformation and the corresponding performance was measured (Figure 4c). The polarization curves at a series of different curvatures show similar shapes, reflecting that the bendable CoP-MNA electrode retains a steady current output even after experiencing extreme bending treatment with negligible decay in catalytic efficiency. Strikingly, CoP-MNA presents no evident structural failure and performance decline after being bent ten times, revealing the highly flexible and considerably recoverable ability. Consequently, the aforementioned facts of versatile shapes and physical integrity for CoP-MNA hold the promise for diverse applications.

2.3. Oxygen Evolution Activity

The opposite reaction initiated on the hydrogen evolution electrode that can availably catalyze the corresponding anodic oxygen evolution process as well, is an import figure of merit to pursue bifunctional water electrolysis electrode and simplify the installation. Hence, the catalytic capacity of CoP-MNA to water oxidation is assessed in the identical electrolyte to HER (1 M KOH). As depicted in **Figure 5**a, it can be expected that Pt electrode show poor activity to produce oxygen. The polarization curve of CoP-MNA manifests a sharp onset potential at approximately 1.50 V, though IrO_2 afford a relatively lower one (about 1.47 V). Noticeably, the anodic current induced by CoP-MNA largely surpasses that of IrO_2 at potentials higher than 1.53 V. The overpotential to deliver a 10 mA cm^{-2} current density, a metric expected for a 10% efficient solar water-splitting device,[58] is only about 1.52 V, which is competitive to that of IrO_2 and ascendant over the reported non-noble active OER electrocatalysts (Table S2, Supporting Information). To examine the kinetics for catalytic OER, the linear fitting of the Tafel plot leads to a low Tafel slope of 65 mV dec^{-1}, even smaller than that of IrO_2 (71 mV dec^{-1}) (Figure 5b). Typically, the electrochemical oxygen evolution in alkaline medium is initialized by OH^- electrosorption on the active sites of the catalyst, suggesting that a catalyst with a benign affinity for OH^- intermediates can promote their formation and equilibrium coverage, thus subsequent step to evolve oxygen will become the rate-determining step, bringing a lower Tafel slope.[41] Accordingly, the decreased Tafel slope for CoP-MNA compared with IrO_2 implies an efficient OER process (Video S2, Supporting Information), coinciding with the higher current density for CoP-MNA relative to IrO_2 in the high potential range. In like manner to HER, OER catalyzed by CoP-MNA is not sensitive to the bending treatment (Figure S8, Supporting Information).

A rotating ring-disk electrode (RRDE) setting is used to verify that the anodic current stems from OER rather than other side reaction and to further estimate the Faradaic efficiency, in which

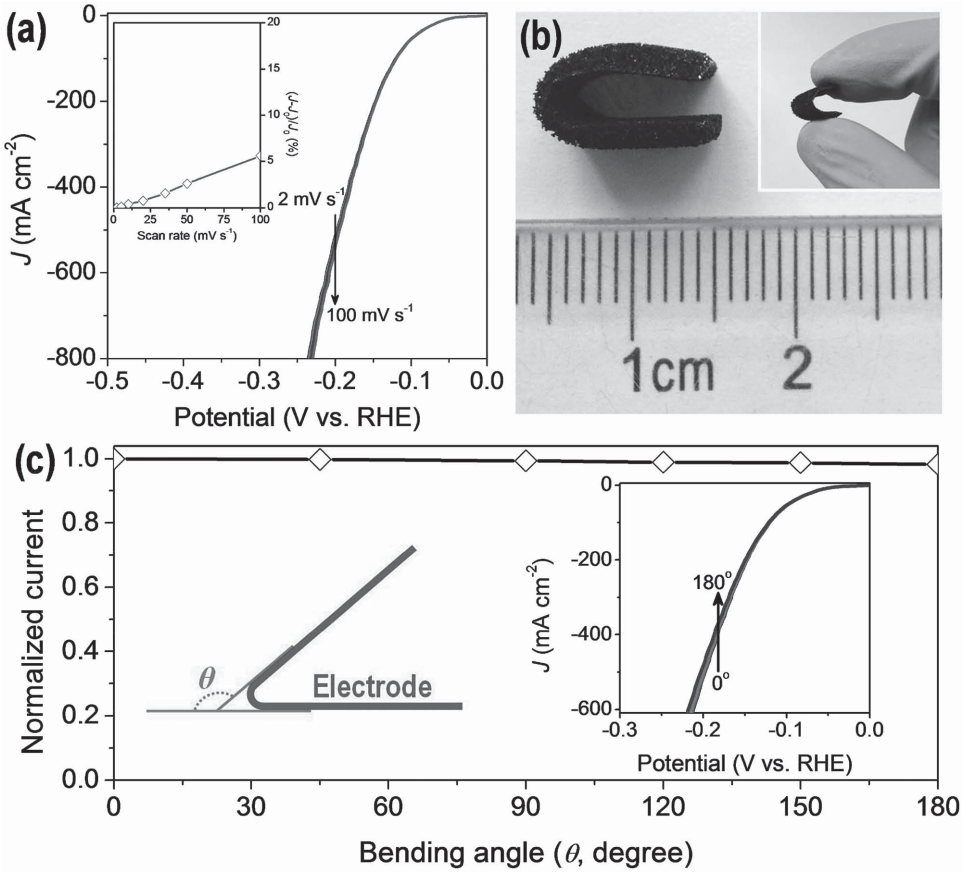

Figure 4. a) Scan-rate-dependent polarization curves for CoP-MNA. Inset of (a): Increased current density percentage versus the scan rate (at –0.2 V). b) Digital photographs of a bent CoP-MNA electrode. c) Variation of the current versus the bending angle. The currents of the original flat electrode are normalized to 1. Inset in (c): Schematic showing of the electrode under a defining the bending angle (left) and polarization curves in different bending angle (right).

a potential of 0.4 V in the oxygen reduction reaction (ORR) region is imposed to ensure that the oxygen formed on the risk sweeping across the surrounding Pt ring can be immediately reduced.[59] With the disk current held at 200 μA, a constant ring current of about 38.9 μA (collection efficiency 0.2) can be identified, indicating that the current catalyzed by CoP-MNA is attribute to the OER process, accompanied with a high Faradaic efficiency of 97.3% (Figure 5c and Figure S9, Supporting Information). Also, the CoP-MNA electrode show excellent electrochemical durability over 32 h continuous experiments (Figure 5d). For the chronopotentiometric response curve, CoP-MNA exhibits a nearly steady potential at about 1.54 V to give a current density of 10 mA cm^{-2}, whereas the notable potential drift for IrO_2 could be due to the loss of active catalysts during the test.

Indeed, other than transition metal oxides, hydroxides, nitrides, phosphates, and chalcogenides, metal phosphides have been seldom explored as OER electrocatalysts.[60,61] Microscopic local structure and constitution of CoP-MNA after OER are elucidated by electron microscopy and X-ray analysis. High-magnification TEM image in **Figure 6**a demonstrates a number of nanoparticles with a size of several nanometers surrounding CoP after water oxidation, possessing clear lattice fringes indicative of registry order or crystallinity. The corresponding interplanar spacing is referred to specific facets of cobalt oxo/hydroxo species.[61–63] In the high-resolution XPS spectra of Co 2p core level (Figure 6b), the post-OER CoP-MNA electrode engenders a negative shift of the main peak (about 1.1 eV) together with weakened shoulders compared with the original state, which signifies a transition of the original Co^{2+} states to higher oxidation states during the anodic reaction process.[60] Two intense bands in the O 1s core level at 531.1 and 529.6 eV can be detected (Figure S10, Supporting Information), corresponding to the abundant surface hydroxyls and oxygen from oxides/hydroxides.[62,63] Besides, the change in the P state is obvious: a single peak located at 133.1 eV is ascribed to phosphate species, as well as the complete disappearance of the phosphide components around the binding energy of 130 eV (Figure S10, Supporting Information).

Taken together, restructuring behavior taking place on CoP-MNA upon anodic potential bias can be available toward OER. During the electrochemical oxygen evolution, the Co^{3+}–OH and Co^{4+}–O moieties within edge-sharing or vertex-sharing Co-oxo/hydroxo molecular units, which resemble the structural configuration of Mn_3CaO_4-type cores of the oxygen-evolving complexes (OEC) in photosystem II, can engender a high density of active sites by introducing molecular cluster structures as active domains, thereby promoting the proton-coupled electron

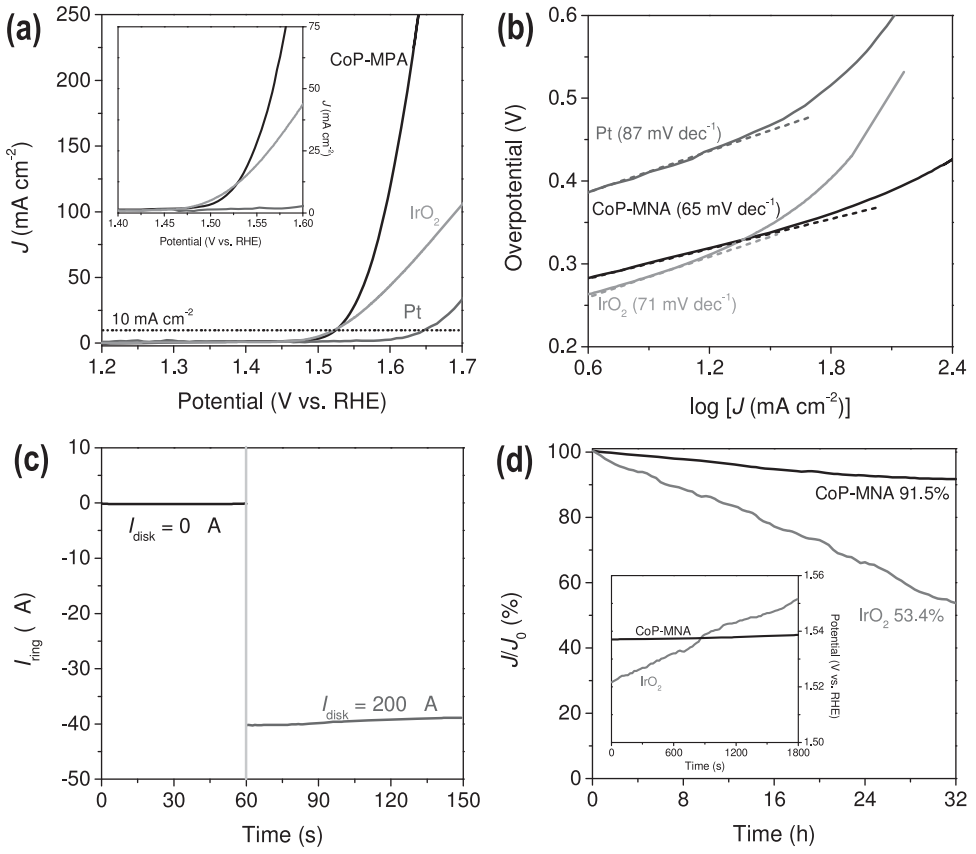

Figure 5. a) LSV polarization curves (2 mV s^{-1} in O_2 saturated 1 M KOH) and b) Tafel plots of CoP-MNA, IrO_2, and Pt for electrocatalytic OER. c) Ring current (*I*) of CoP-MNA coated on a RRDE at a constant ring potential of 0.40 V. d) Chronoamperometric response measured at a potential of 1.52 V. Inset in (d): Chronopotentiometric response at a constant current density of 10.0 mA cm^{-2} of CoP-MNA and IrO_2.

transfer (PCET).[64,65] As such, the enhanced water oxidation kinetics can be related to the abundance of such local molecular units within the local structures, while CoP nanorods can act as conductive supports to further facilitate electron transfer to the exterior active components. In addition, since the phosphate groups are known to evaluate PCET process,[42,66] the presence of surface-bound phosphate moieties may boost the oxygen evolution kinetics as well. Moreover, the well-defined porosity and nanoarray configuration are indispensable to render accessible active sites, fast diffusion of reactants/products, and rapid PCET. Consequently, the synergistic effect from these sides makes contribution to the improved oxygen evolution performance.

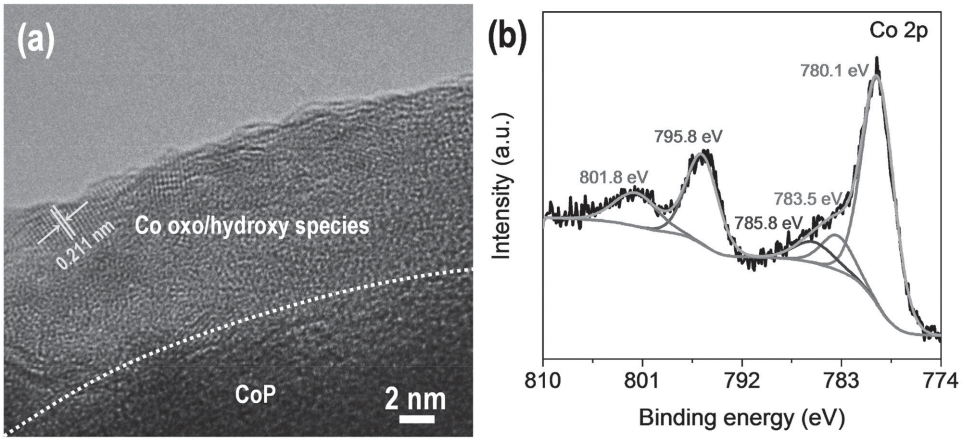

Figure 6. a) HRTEM image and b) Co 2p core level XPS spectra of CoP-MNA after electrochemical OER.

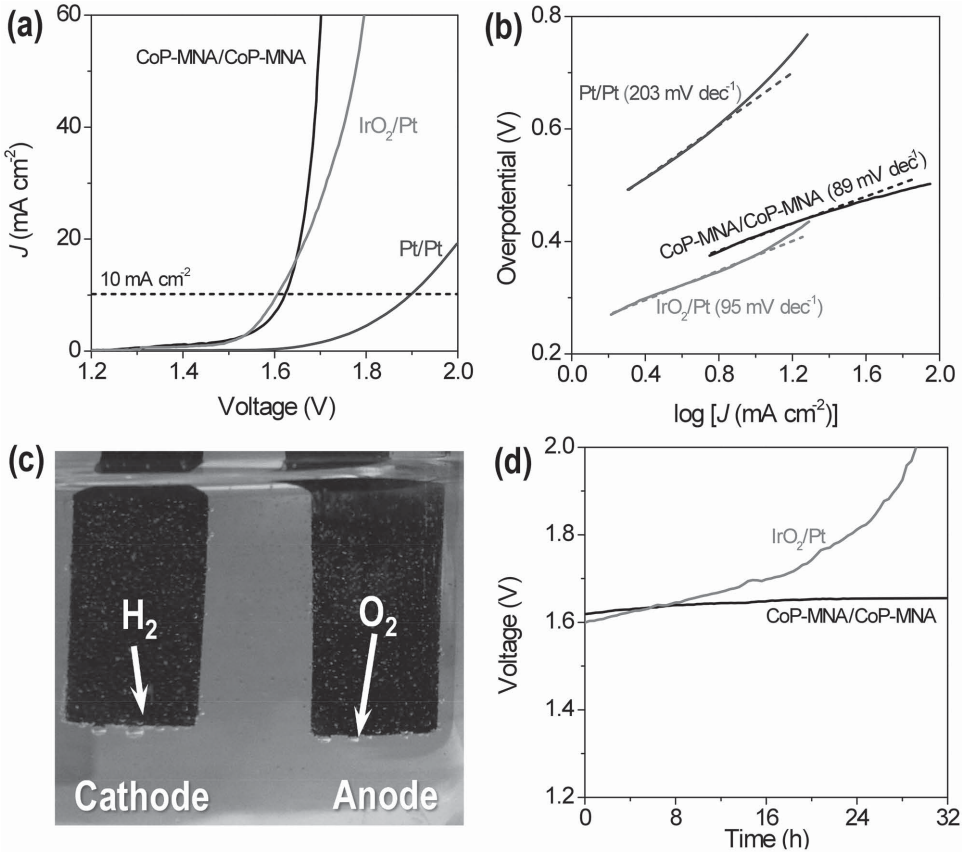

Figure 7. a) Polarization curves of a two-electrode alkaline electrolyzer using CoP-MNA/Co-MNA, IrO_2/Pt, and Pt/Pt at a sweeping rate of 2 mV s^{-1} in 1 M KOH. b) Tafel plots and the associated linear fittings (dotted lines). c) A representative photograph of the system depicting H_2 (left) and O_2 (right) generation during overall water electrolysis. d) Galvanostatic water electrolysis at a stationary current density of 10 mA cm^{-2} over the course of 32 h for CoP-MNA/CoP-MNA and IrO_2/Pt.

2.4. Overall Water Splitting

Depending on the results above, it is reasonably anticipated that the CoP-MNA electrode can serve as a bifunctional electrocatalyst for overall water splitting to get a further step close to the real applicability. A preliminary estimation is taken using a single electrolyzer equipped with a two-electrode setup, in which the as-synthesized CoP-MNA electrode functions as both anode and cathode (marked as CoP-MNA/CoP-MNA) (**Figure 7**a). A current density of 10 mA cm^{-2} can be gained at a cell voltage of 1.62 V, representing a combined overpotential of 390 mV for full water oxidation and reduction. Of note, noble IrO_2 is well-established catalyst for OER and Pt for HER, the coupling of IrO_2 as anode and Pt as cathode is predicted to obtain an outstanding integrated catalytic system. Although the overall water electrolysis polarization profile for the CoP-MNA/CoP-MNA electrode exhibits a slightly larger onset potential than the benchmark combination, but quickly catches up with the IrO_2/Pt when the potential passes through 1.65 V. This is attributable to a lower Tafel slope of CoP-MNA/CoP-MNA (89 mV dec^{-1}) than that of IrO_2/Pt (95 mC dec^{-1}), favoring facile kinetics and bubble releasing process (Figure 7b,c). The stability measurements over the course of 32 h also offer advantages of CoP-MNA over the noble-metal-based electrocatalysts (Figure 7d). With a slight lower beginning voltage of 1.62 V to deliver a 10 mA cm^{-2} current density, the voltage then stabilizes around 1.65 V to supply persistent water-splitting current, which surpasses the precious IrO_2/Pt couple after about 6 h reaction.

3. Conclusions

In summary, cobalt phosphide mesoporous nanorod arrays directly deposited on to nickel foam through readily scalable and cost-effective electrochemical strategy can function as a 3D flexible electrode for overall water splitting. The considerable HER and OER performance with favorable kinetics and robust stability can rival the state-of-the-art catalysts, which can be intimately related to the unique electrode configuration and porosity that ensures structural connections and improved mass/charge transport. The dual functionality is capable of the direct use as electrodes for both cathode and anode in an alkaline water eletrolyzer, realizing a current density of 10 mA cm^{-2} at an overpotential of 390 mV with strong durability. This work will pave an alternative pathway for designing a large variety of bifunctional flexible electrodes constructed from nonprecious active catalysts, aiming at water-electrolysis devices and other emerging renewable energy conversion systems.

Supporting Information

Supporting Information is available from the Wiley Online Library or from the author.

Acknowledgements

This work was supported by the National Natural Science Foundation of China (21421001, 21573115), the Natural Science Foundation of Tianjin (15JCZDJC37100), the MOE Innovative Team (IRT13022), and the 111 project (B12015).

Received: August 29, 2015
Revised: September 27, 2015
Published online: November 6, 2015

[1] D. G. Nocera, *Acc. Chem. Res.* **2012**, *45*, 767.
[2] M. S. Dresselhaus, I. L. Thomas, *Nature* **2001**, *414*, 332.
[3] Z. Q. Peng, S. A. Freunberger, Y. H. Chen, P. G. Bruce, *Science* **2012**, *337*, 563.
[4] T. Y. Ma, J. Ran, S. Dai, M. Jaroniec, S. Z. Qiao, *Angew. Chem. Int. Ed.* **2015**, *54*, 4646.
[5] K. Zeng, D. Zhang, *Prog. Energy Combust. Sci.* **2010**, *36*, 307.
[6] J. Suntivich, K. J. May, H. A. Gasteiger, J. B. Goodenough, Y. Shao-Horn, *Science* **2011**, *334*, 1383.
[7] X. Zou, Y. Zhang, *Chem. Soc. Rev.* **2015**, *44*, 5148.
[8] S. Park, Y. Shao, J. Liu, Y. Wang, *Energy Environ. Sci.* **2012**, *5*, 9331.
[9] Y. Jiao, Y. Zheng, M. Jaroniec, S. Z. Qiao, *Chem. Soc. Rev.* **2015**, *44*, 2060.
[10] T. Y. Ma, S. Dai, M. Jaroniec, S. Z. Qiao, *J. Am. Chem. Soc.* **2014**, *136*, 13925.
[11] G. S. Hutchings, Y. Zhang, J. Li, B. T. Yonemoto, X. Zhou, K. Zhu, F. Jiao, *J. Am. Chem. Soc.* **2015**, *137*, 4223.
[12] F. Song, X. Hu, *J. Am. Chem. Soc.* **2014**, *136*, 16481.
[13] Q. Liu, J. Tian, W. Cui, N. Cheng, A. M. Asiri, X. Sun, *Angew. Chem. Int. Ed.* **2014**, *53*, 6710.
[14] E. J. Popczun, C. G. Read, C. W. Roske, N. S. Lewis, R. E. Schaak, *Angew. Chem. Int. Ed.* **2014**, *53*, 5427.
[15] J. Bao, X. Zhang, B. Fan, J. Zhang, M. Zhou, W. Yang, X. Hu, H. Wang, B. Pan, Y. Xie, *Angew. Chem. Int. Ed.* **2015**, *54*, 7399.
[16] Z. Peng, D. Jia, A. M. Al-Enizi, A. A. Elzatahry, G. Zheng, *Adv. Energy Mater.* **2015**, *5*, 1402031.
[17] D. Kong, H. Wang, Z. Lu, Y. Cui, *J. Am. Chem. Soc.* **2014**, *136*, 4897.
[18] J. Ren, M. Antonietti, T. P. Fellinger, *Adv. Energy Mater.* **2015**, *5*, 1401660.
[19] M. Gong, W. Zhou, M. C. Tsai, J. Zhou, M. Guan, M. C. Lin, B. Zhang, Y. Hu, D. Y. Wang, J. Yang, S. J. Pennycook, B. J. Hwang, H. Dai, *Nat. Commun.* **2014**, *5*, 4695.
[20] J. Luo, J. H. Im, M. T. Mayer, M. Schreier, M. K. Nazeeruddin, N. G. Park, S. D. Tilley, H. J. Fan, M. Grätzel, *Science* **2014**, *345*, 1593.
[21] X. Zou, X. Huang, A. Goswami, R. Silva, B. R. Sathe, E. Mikmeková, T. Asefa, *Angew. Chem. Int. Ed.* **2014**, *53*, 4372.
[22] Y. Sun, C. Liu, D. C. Grauer, J. Yano, J. R. Long, P. Yang, C. J. Chang, *J. Am. Chem. Soc.* **2013**, *135*, 17699.
[23] M. R. Gao, J. X. Liang, Y. R. Zheng, Y. F. Xu, J. Jiang, Q. Gao, J. Li, S. H. Yu, *Nat. Commun.* **2015**, *6*, 5982.
[24] G. S. Hutchings, Y. Zhang, J. Li, B. T. Yonemoto, X. Zhou, K. Zhu, F. Jiao, *J. Am. Chem. Soc.* **2015**, *137*, 4223.
[25] M. S. Burke, M. G. Kast, L. Trotochaud, A. M. Smith, S. W. Boettcher, *J. Am. Chem. Soc.* **2015**, *137*, 3638.
[26] H. Jin, J. Wang, D. Su, Z. Wei, Z. Pang, Y. Wang, *J. Am. Chem. Soc.* **2015**, *137*, 2688.
[27] H. Wang, H. K. Lee, Y. Deng, Z. Lu, P. C. Hsu, Y. Liu, D. Lin, Y. Cui, *Nat. Commun.* **2015**, *6*, 7261.
[28] S. Chen, J. Duan, M. Jaroniec, S. Z. Qiao, *Adv. Mater.* **2014**, *26*, 2925.
[29] J. Duan, S. Chen, M. Jaroniec, S. Z. Qiao, *ACS Nano* **2015**, *9*, 931.
[30] M. S. Faber, R. Dziedzic, M. A. Lukowski, N. S. Kaiser, Q. Ding, S. Jin, *J. Am. Chem. Soc.* **2014**, *136*, 10053.
[31] N. Kornienko, J. Resasco, N. Becknell, C. M. Jiang, Y. S. Liu, K. Nie, H. Sun, J. Guo, S. R. Leone, P. Yang, *J. Am. Chem. Soc.* **2015**, *137*, 7448.
[32] S. Chen, J. Duan, P. Bian, Y. Tang, R. Zheng, S. Z. Qiao, *Adv. Energy Mater.* **2015**, *5*, 1500936.
[33] S. Chen, J. Duan, J. Ran, S. Z. Qiao, *Adv. Sci.* **2015**, *2*, 1400015.
[34] Y. Zheng, Y. Jiao, S. Z. Qiao, *Adv. Mater.* **2015**, *27*, 5372.
[35] J. Duan, S. Chen, M. Jaroniec, S. Z. Qiao, *ACS Catal.* **2015**, *9*, 5207.
[36] J. H. Heo, D. Song, H. J. Han, S. Y. Kim, J. H. Kim, D. Kim, H. W. Shin, T. K. Ahn, C. Wolf, C. W. Lee, S. H. Im, *Adv. Mater.* **2015**, *27*, 3424.
[37] L. Liu, Z. Niu, L. Zhang, W. Zhou, X. Chen, S. Xie, *Adv. Mater.* **2014**, *26*, 4855.
[38] E. J. Popczun, C. G. Read, C. W. Roske, N. S. Lewis, R. E. Schaak, *Angew. Chem. Int. Ed.* **2014**, *53*, 5427.
[39] J. Tian, Q. Liu, A. M. Asiri, X. Sun, *J. Am. Chem. Soc.* **2014**, *136*, 7587.
[40] N. Jiang, B. You, M. Sheng, Y. Sun, *Angew. Chem. Int. Ed.* **2015**, *54*, 6251.
[41] Y. Yang, H. Fei, G. Ruan, J. M. Tour, *Adv. Mater.* **2015**, *27*, 3175.
[42] M. W. Kanan, Y. Surendranath, D. G. Nocera, *Chem. Soc. Rev.* **2009**, *38*, 109.
[43] J. A. Plambeck, A. J. Bard, L. Henning, *Encyclopedia of Electrochemistry of the Elements*, Vol. 3, Taylor & Francis Group, Abington, Oxon, UK **1973**.
[44] D. Yang, J. Zhu, X. Rui, H. Tan, R. Cai, H. E. Hoster, D. Y. W. Yu, H. H. Hng, Q. Yan, *ACS Appl. Mater. Interfaces* **2013**, *5*, 1093.
[45] J. Cabana, L. Monconduit, D. Larcher, M. R. Palacín, *Adv. Mater.* **2010**, *22*, E170.
[46] D. Gu, F. Schüth, *Chem. Soc. Rev.* **2014**, *43*, 313.
[47] X. J. Liu, Z. Chang, L. Luo, T. H. Xu, X. D. Lei, J. F. Liu, X. M. Sun, *Chem. Mater.* **2014**, *26*, 1889.
[48] L. Shen, Q. Che, H. Li, X. Zhang, *Adv. Funct. Mater.* **2014**, *24*, 2630.
[49] D. U. Lee, J. Y. Choi, K. Feng, H. W. Park, Z. Chen, *Adv. Energy Mater.* **2014**, *4*, 1301389.
[50] X. Yang, A. Y. Lu, Y. Zhu, M. N. Hedhili, S. Min, K. W. Huang, Y. Han, L. J. Li, *Nano Energy* **2015**, *15*, 634.
[51] A. P. Grosvenor, S. D. Wik, R. G. Cavell, A. Mar, *Inorg. Chem.* **2005**, *44*, 8988.
[52] H. Vrubel, X. Hu, *Angew. Chem. Int. Ed.* **2012**, *51*, 12703.
[53] S. A. Vilekar, I. Fishtik, R. Datta, *J. Electrochem. Soc.* **2010**, *157*, B1040.
[54] E. Skúlason, V. Tripkovic, M. E. Björketun, S. Gud-mundsdóttir, G. Karlberg, J. Rossmeisl, T. Bligaard, H. Jónsson, J. K. Nørskov, *J. Phys. Chem. C* **2010**, *114*, 18182.
[55] A. W. Burns, K. A. Layman, D. H. Bale, M. E. Bussell, *Appl. Catal. A* **2008**, *343*, 68.
[56] Z. Huang, Z. Z. Chen, Z. B. Chen, C. Lv, M. G. Humphrey, C. Zhang, *Nano Energy* **2014**, *9*, 373.
[57] Y. Zhao, R. Nakamura, K. Kamiya, S. Nakanishi, K. Hashimoto, *Nat. Commun.* **2013**, *4*, 2390.
[58] C. C. L. McCrory, S. Jung, J. C. Peters, T. F. Jaramillo, *J. Am. Chem. Soc.* **2013**, *135*, 16977.
[59] T. Nakagawa, N. S. Bjorge, R. W. Murray, *J. Am. Chem. Soc.* **2009**, *131*, 15578.

[60] J. Ryu, N. Jung, J. H. Jang, H. J. Kim, S. J. Yoo, *ACS Catal.* **2015**, *5*, 4066.
[61] L. A. Stern, L. Feng, F. Song, X. Hu, *Energy Environ. Sci.* **2015**, *8*, 2347.
[62] J. Yang, H. Liu, W. N. Martens, R. L. Frost, *J. Phys. Chem. C* **2010**, *114*, 111.
[63] M. C. Biesingera, B. P. Payne, A. P. Grosvenor, L. W. M. Lau, A. R. Gerson, R. Smart, *Appl. Surf. Sci.* **2011**, *257*, 2717.
[64] S. Cobo, J. Heidkamp, P. A. Jacques, J. Fize, V. Fourmond, L. Guetaz, B. Jousselme, V. Ivanova, H. Dau, S. Palacin, M. Fontecave, V. Artero, *Nat. Mater.* **2012**, *11*, 802.
[65] J. B. Gerken, J. G. McAlpin, J. Y. C. Chen, M. L. Rigsby, W. H. Casey, R. D. Britt, S. S. Stahl, *J. Am. Chem. Soc.* **2011**, *133*, 14431.
[66] Q. Yin, J. M. Tan, C. Besson, Y. V. Geletii, D. G. Musaev, A. E. Kuznetsov, Z. Luo, K. I. Hardcastle, C. L. Hill, *Science* **2010**, *328*, 342.